





Corrosion behavior of a novel Mg–13Li–X alloy with different grain sizes by rapid solidification rate

Bao-Liang Wu , Bing Chen, Cheng-Wei Wang,
Jing-Ye Jiao, Qi-Chao Shen, Tie-Tao Zhou* 

Received: 27 August 2014/Revised: 25 October 2014/Accepted: 20 August 2015/Published online: 18 September 2015
© The Nonferrous Metals Society of China and Springer-Verlag Berlin Heidelberg 2015

Abstract As degradable biomaterials, the higher degradation rate of Mg–Li alloys in the physiological environment is the main challenge for the implant applications. In order to try and overcome this limitation, the present work was dedicated to studying the corrosion behavior of a novel Mg–13Li–X alloy fabricated by a rapid solidification process (RSP). The special Mg–13Li–X alloy was immersed in Hank's balanced salt solution (HBSS), and the influence of immersion time on corrosion rate was analyzed. X-ray diffraction (XRD) and scanning electron microscopy (SEM), complemented with electrochemical techniques such as potentiodynamic polarization curves and electrochemical impedance spectroscopy, were applied. Microstructural characterization indicates that the mean grain sizes of RSP Mg–13Li–X alloy are 4.2, 8.2 and 12.7 μm with the solidification rate decreasing. By contrast, the conventional as-cast Mg–13Li–X alloy has an average grain size of about 150 μm . The results of electrochemical test indicate that the sample with 4.2 μm in grain size has the most positive corrosion potential (E_{corr}) of -1.354 V and the minimum corrosion current (I_{corr}) of 5.830×10^{-7} $\text{A}\cdot\text{cm}^{-2}$ after immersion for 2 h in HBSS. Therefore, the finest grain size can improve the polarization resistance of the alloy, reduce its corrosion current density and increase its corrosion resistance. However, because the weak layer of the corrosion product which consists of $\text{Mg}(\text{OH})_2$ does not afford strong

protection, the corrosion resistance becomes worse after immersion for longer periods.

Keywords Biomedical Mg–Li alloys; Rapid solidification; Grain size; Bio-environment immersion; Corrosion behavior

1 Introduction

Mg-based alloys have attracted broad attention due to their unique properties, such as their low density ($1.35\text{--}1.65$ $\text{g}\cdot\text{cm}^{-3}$) and high specific strength. Therefore, Mg and its alloys can be widely used in computer and mobile equipment, weapon industries and aerospace applications [1–3]. Furthermore, Mg alloys also have great potential for use in stent applications and for bone implants because their many properties are similar to those of human bones, such as their low density, Young modulus (40–45 GPa) and yield strength [4–6]. Therefore, the effect of the stress-shielding phenomenon can be minimized by using Mg alloys as the implants instead of stainless steel and Ti alloys [7]. In recent years, many studies have reported on the fusion casting and processing technologies, microstructures and mechanical properties of Mg–Li alloys [8]. The content of Li is the decisive factor to vary the structures of Mg–Li alloys. When the content of Li is more than 10.3 wt%, the ductility of Mg alloys increases because the crystalline structure varies from hcp Mg to bcc Mg. Adding Zn and Al (such as 1 wt% Zn and 3 wt% Al) can significantly improve the mechanical properties of pure Mg [9].

Mg–Li alloys are promising complements to ceramic materials, high polymer materials and some other biomaterial alloys such as 316 L stainless steel, Co–Cr alloy, mainly due to their excellent degradability. As degradable biomaterials, however, their poor corrosion resistance

B.-L. Wu, C.-W. Wang, J.-Y. Jiao, Q.-C. Shen, T.-T. Zhou*
School of Materials Science and Engineering, Beihang
University, Beijing 100191, China
e-mail: 04380@buaa.edu.cn

B. Chen
Vascular Department, Second Affiliated Hospital, Medicine
School of Zhejiang University, Hangzhou 310052, China

prevents the wide use of Mg–Li alloys [10]. Hence, it is worthwhile for researchers to study the corrosion behavior and improve the corrosion resistance of Mg–Li alloys. During previous investigations, the corrosion behavior and mechanism of Mg–Al alloys were studied: oxidation films consisting of corrosion products were generated on the surfaces, and pitting corrosion was promoted by exposure to Cl^- [11–13]. Many methods were applied to improve the corrosion resistance of Mg–Al alloys, including organic coating, anodizing, ion implantation and the use of conversion coatings [14]. However, only a few studies on corrosion behavior of Mg–Li alloys have been reported [15].

In consideration of the previous research in earlier investigations, the corrosion mechanism of the forged Mg–13Li–X alloys was localized corrosion and the corrosion resistance of the forged alloy exhibited no obvious improvement [16]. Several studies were reported that the microstructures and grain sizes of Mg alloys controlled its corrosion behavior, and the amount and distribution of intermetallic phases are other important influencing factors [17, 18]. Li et al. [18] proposed microcrystallization as a new method to modify the study of corrosion behavior and improve its corrosion resistance in chloride solutions.

In the present investigation, the microstructure and corrosion behavior of the novel Mg–13Li–X alloy with different grain sizes were studied. Through the rapid solidification process (RSP), it is possible to produce fine-grain Mg–13Li–X alloys in order to improve the mechanical properties and corrosion behavior in a manner that could not be achieved by conventional ingot processing [19]. Attempts to evaluate the relationship between corrosion resistance and grain size were proposed in this study. The aim of the work is to evaluate the effect of different grain sizes achieved by rapid solidification process (RSP) on microstructure and corrosion behavior of the novel Mg–13Li–X alloy, and to improve its corrosion resistance.

2 Experimental

2.1 Materials

The chemical composition of the studied alloy is Mg–13Li–3Al–1Zn–0.5Ca–0.5Sr (wt%). The preparation of the investigated material was divided into two parts. Firstly, the alloy with a chemical composition of Mg–13Li–X (wt%) was prepared from pure Mg, Li, Al, Zn, Ca and Sr, melted in the vacuum furnace and cast in a low-carbon steel crucible under a protective gas of Ar [10]. The alloy ingots were remelted twice in the furnace to ensure compositional homogeneity. Subsequently, the alloy ingots were remelted by an induction furnace. Rods with a diameter of $\Phi 3$, $\Phi 4$ and

$\Phi 6$ mm were prepared by casting from a graphite crucible protected by SF_6 into a special copper die. The similar way to fabricate Mg alloys could form bulk metallic glass with the cooling rate of $10^3 \text{ }^\circ\text{C}\cdot\text{s}^{-1}$ or high [20]. These samples with a diameters of $\Phi 3$, $\Phi 4$ and $\Phi 6$ mm were termed as Samples M3, M4 and M6, respectively.

The size of the special copper die was $10 \text{ cm} \times 8 \text{ cm} \times 6 \text{ cm}$. There were three different holes with the diameters of $\Phi 3$, $\Phi 4$ and $\Phi 6$ mm in the die. The volume of M6 was four times as large as that of M3 and twice as large as that of M4. Therefore, their solidification rates also had a proportional relationship.

2.2 Microstructural characterization

The microstructures of the RSP alloy samples were observed by optical microscopy (OM, Leica DM4000 M) and scanning electron microscopy (SEM, CS 3400). The samples were prepared by grinding on SiC paper (3000 grade), followed by mechanical polishing with $1 \text{ }\mu\text{m}$ Al_2O_3 paste and short final polishing using colloidal silica. The grain structure was finally revealed by etching, using a solution of 3 vol% nitric acid for 3–5 s, then thoroughly flushed with alcohol and dried by a cold air blast. The grain sizes were calculated by SISC-IAS image analysis software.

X-ray diffraction (XRD, Rigaku D/max IIIA, Cu $K\alpha$) was utilized to identify the crystalline phases of the rapidly solidified samples. Energy-dispersive spectroscopy (EDS, INCA Penta FET-x3) was used to investigate the distribution of all the elements except lithium in the alloy. After immersion tests in the Hank's balanced salt solution (HBSS), compositional and microstructural characterizations of the alloy surface were carried out using XRD and SEM, respectively. Before the observation of the exposed alloy samples, another solution was used to eliminate corrosion products: 200 g CrO_3 , 10 g AgNO_3 and 20 g $\text{Ba}(\text{NO}_3)_2$ were added to distilled water to prepare 1000 ml solution. The immersed samples were sonic oscillated in the solution for about 1 min at $(23.0 \pm 0.5) \text{ }^\circ\text{C}$.

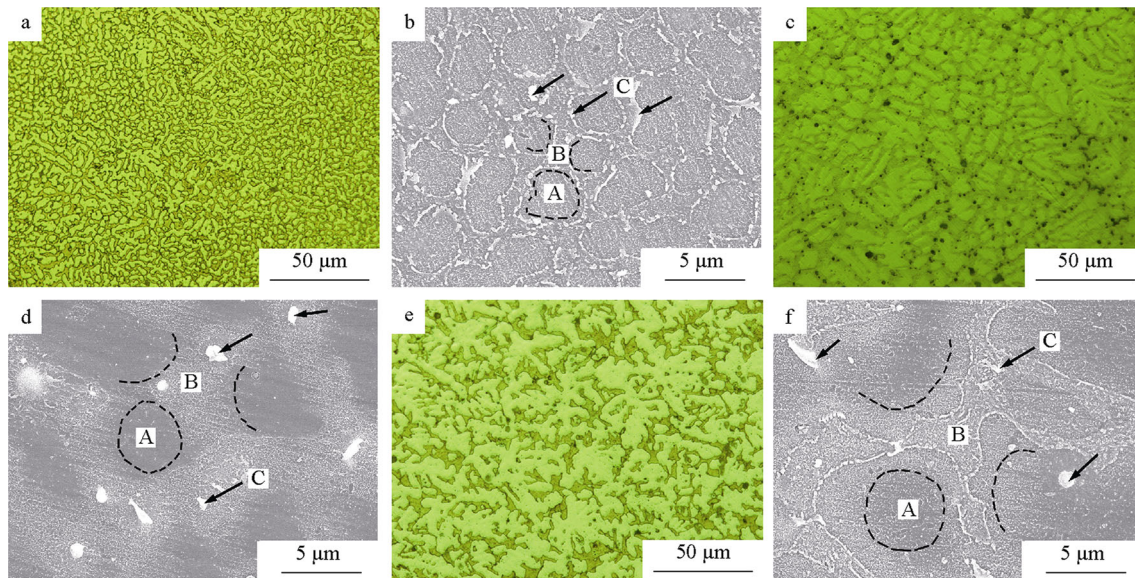
2.3 Corrosive medium and electrochemical techniques

The corrosive medium is HBSS, and its specific composition is shown in Table 1. Electrochemical impedance spectroscopy (EIS, CHI660A) is a technique with a small perturbative signal, which causes little damage to the surface of the sample. In addition to providing an indication of the relative corrosion rate, EIS allows the corrosion mechanism to be characterized by analyzing the impedance response [21].

A typical three-electrode system consisting of a platinum grid with a large surface area as the counter electrode

Table 1 Chemical compositions of HBSS (g·L⁻¹)

NaCl	KCl	CaCl ₂	NaHCO ₃	C ₆ H ₆ O ₆	KH ₂ PO ₄	MgCl ₂ ·6H ₂ O	MgSO ₄ ·7H ₂ O	Na ₂ HPO ₄ ·12H ₂ O
8.00	0.40	0.14	0.35	1.00	0.10	0.10	0.20	0.06

**Fig. 1** OM images (a, c, e) and SEM images (b, d, f) of Samples: a, b M3; c, d M4; e, f M6

saturated calomel electrode (SCE) as the reference electrode and a specimen (with a specific exposed area) was used as the working electrode. Cross sections were cut from the fabricated samples with different diameters of $\Phi 3$, $\Phi 4$ and $\Phi 6$ mm. The body of these rods was covered with chloroprene rubber, leaving only a specific area in contact with the solution. Preparation of the samples for electrochemical experiments was related to the preparation of OM and SEM samples. These samples were cleaned in distilled water in ultrasonic bath and dried in a cold air blast.

Two types of electrochemical experiments were conducted: EIS and potentiodynamic polarization near the corrosion potential (E_{corr}). Impedance spectra were generated over the frequency range of 100 mHz–10 kHz using a sinusoidal wave of 10 mV in amplitude. The potentiodynamic polarization experiments were carried out on an electrochemical workstation (CHI660A). Both the potentiodynamic polarization experiments and the immersion tests were conducted in HBSS at (37.0 ± 0.5) °C controlled by a water bath (HH-W420). The practical scan rate of the potentiodynamic polarization experiments was $0.02 \text{ V}\cdot\text{s}^{-1}$. The potentiodynamic polarization response was measured during immersion in HBSS for 2, 24, 48 and 72 h.

3 Results and discussion

3.1 Microstructure analysis

As shown in Fig. 1a, c, e, the matrix of RSP Mg–13Li–X alloy consists mainly of single β -Li phase, as predicted by the binary phase diagram [22, 23]. It can be seen from Fig. 1a, c, e that these samples with different cooling rates all have dendritic microstructures. The dendritic microstructures can be strong evidence of a rapid cooling rate. As affected by RSP, the grain sizes are refined observably (Fig. 1). The as-cast Mg–13Li–X alloy has an average grain size of about $150 \mu\text{m}$ [24], while the mean grain sizes of RSP Mg–13Li–X alloy are 4.2, 8.2 and $12.7 \mu\text{m}$ for Samples M3, M4 and M6, respectively.

In Fig. 1b, Area A is the primary phase consisting of single phase β -Li. The primary phase nucleates during the initial period of solidification and grows as the solidification of Mg–13Li–X alloy is proceeding. On account of the rapid solidification rate, the degree of supercooling on solid–liquid interface is sufficiently high, which produces dendritic microstructures. The eutectic phase or pseudo-eutectic phase (Area B) starts to be generated around Area A after the primary phase develops. EDS analysis shows that alloying elements such as Al, Zn and Ca gather in the

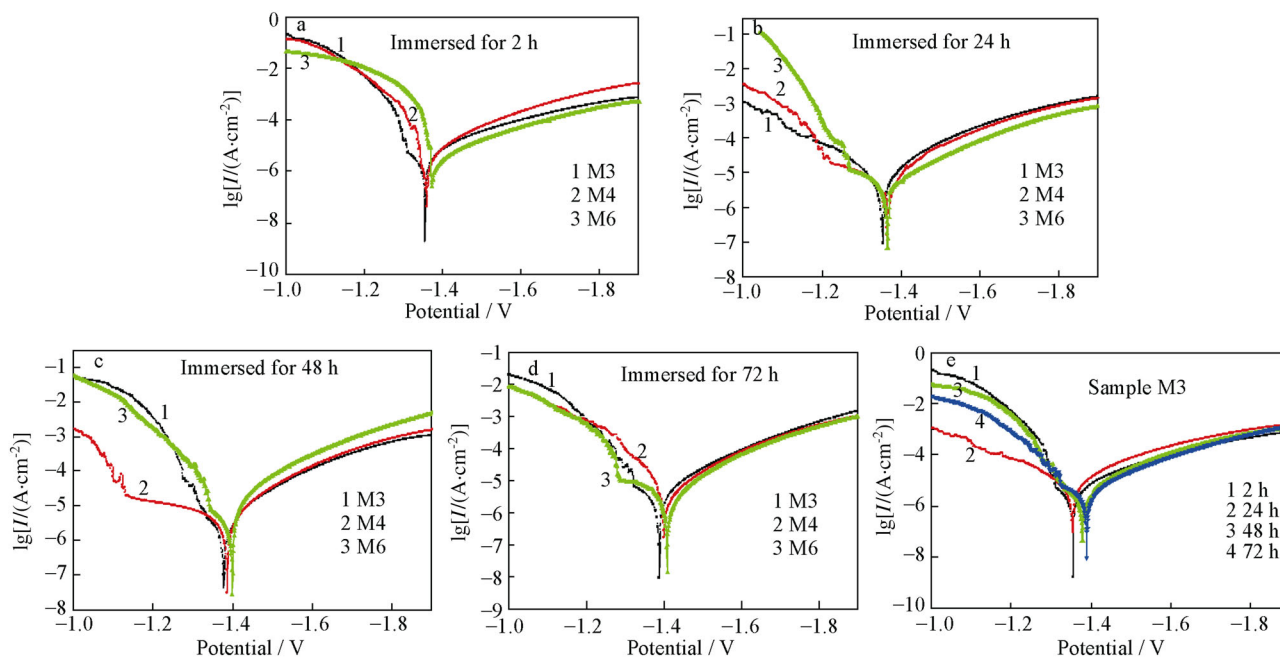


Fig. 2 Polarization curves of Samples M3, M4 and M6 immersed in HBSS for **a** 2 h, **b** 24 h, **c** 48 h and **d** 72 h; and **e** polarization curves of Sample M3 immersed in solution for different time

eutectic phase or pseudo-eutectic phase (Area B). Because Area B is generated during the last period of solidification and there is no surplus alloy liquid to be supplemented into Area B, its microstructure is less compact than that of Area A. Area C is another phase formed with the primary phase, but it dissociates from the primary phase to the eutectic phase. The main composition of Area C is $Al_{0.58}Mg_{0.42}$ which can be determined by EDS. By comparing Fig. 1b, d, f, it can be observed that with the decrease in the cooling rate, the degree of supercooling of the solid–liquid interface is lower, resulting in a gradually larger area of the eutectic phase. The proportion of the primary phase to the eutectic phase is different with different solidification rates.

3.2 Potentiodynamic polarization

Figure 2 shows the polarization curves of RSP Mg–13Li–X alloy with different immersion time, and Table 2 summarizes the parameters of the polarization curves. All the cathodic polarization curves are similar mostly, while the anodic branches are evidently different. This is because immersion time and solidification rate have few effects on the cathodic polarization behavior. Since the effects of oxygen on cathodic polarization are very small, hydrogen evolution is the main cathodic process, and plenty of bubbles are formed on the electrode surface.

The corrosion velocity of the novel Mg–13Li–X alloy in HBSS is controlled mostly by anodic process. In Fig. 2, the corrosion potential (E_{corr}) shifts toward the positive

Table 2 Corrosion data of RSP Mg–13Li–X alloy with different immersion time

Time/h	Grain size/ μm	$I_{corr}/(A \cdot cm^{-2})$	E_{corr}/V
2	4.2	5.830×10^{-7}	–1.354
	8.2	1.494×10^{-6}	–1.363
	12.7	8.169×10^{-6}	–1.375
24	4.2	8.136×10^{-7}	–1.355
	8.2	1.781×10^{-6}	–1.367
	12.7	1.627×10^{-5}	–1.370
48	4.2	1.001×10^{-6}	–1.382
	8.2	2.800×10^{-6}	–1.390
	12.7	2.148×10^{-5}	–1.401
72	4.2	7.123×10^{-6}	–1.389
	8.2	7.160×10^{-6}	–1.406
	12.7	4.315×10^{-5}	–1.409

direction with an increase in solidification rate for different immersion time. It can be concluded that the solidification rate is the most important influencing factor on the corrosion resistance in this test. Therefore, Sample M3 with the most rapid solidification rate has the highest corrosion resistance. In Fig. 2b, c, d, obvious passivation stage can be observed from the anodic curves. Passivation can be attributable to the protective effect of the corrosion product layer. As the immersion time and solidification rate change, the passivation stage is different. Figure 2e shows the

polarization curves of Sample M3 in HBSS for different immersion time. The corrosion potential (E_{corr}) turns toward more negative values with immersion time increasing. A similar result is observed in the polarization curves for Samples M4 and M6.

Table 2 shows that corrosion becomes more serious when the immersion time increases from 2 to 72 h. When the immersion time is 2 h, the corrosion currents (I_{corr}) of all samples have the minimum values. The result can be explained by that the corrosion products of the Mg–13Li–X alloy are loose and uncompact [25]. The layer consisting of corrosion products cannot afford strong protective effect to the surfaces of all three samples. In addition, bubble formation is observed, and the test temperature is 37 °C. These factors all can contribute to the falling off of loose corrosion product layer and the increase in corrosion current density. Moreover, the white precipitate observed in HBSS after electrochemical experiments can support this explanation.

3.3 Electrochemical impedance spectroscopy

Figure 3 shows Nyquist impedance plots of Samples M3, M4 and M6 after immersion for 2 h (Fig. 3a), 24 h (Fig. 3b), 48 h (Fig. 3c) and 72 h (Fig. 3d) in HBSS, respectively. In these plots, a well-defined capacitive loop at medium and low frequencies is observed for all immersion time. There is another small capacitive loop in the plots at high frequency after immersion for 24, 48 and 72 h. However, the plot after immersion for 2 h does not

exhibit the small capacitive loop. The capacitive loop at medium and low frequencies is attributed to charge transfer (probably formation of Mg^{2+}) and the double-layer capacitance of the electrode. The capacitive loop at high frequency is attributed to a film effect caused by the existence of corrosion product layer.

In Fig. 3, by comparing the diameters of the capacitive loops at medium- and low-frequency regions for different immersion time, Sample M3 has higher diameters than Samples M4 and M6. Evidently, the corrosion resistance improves as the alloy solidification rate increases. This result indicates that grain size can be a significant influencing factor on corrosion performance and corrosion resistance improves as the grain size decreases. As shown in Fig. 1, finer grain sizes mean that the area of the eutectic phase is smaller, so the sample with the finest grain size has the best corrosion performance.

As for Sample M3, the impedance plots for different immersion time are presented in Fig. 3e. There is little variation in the loops for 2–24-h immersion because the shape of the Nyquist impedance plots after immersion for 2 and 24 h changes and the corrosion product layer cannot prevent corrosion attacking at the surface. However, the diameters of the capacitive loops at medium and low frequencies decrease with immersion time increasing from 24 to 48 h. This phenomenon indicates that the surface of this sample is attacked and charge transfer (probably Mg dissolution to Mg^{2+}) becomes easier. When the immersion time increases from 48 to 72 h, the diameters of the impedance plots are slightly smaller. This is perhaps because the surface

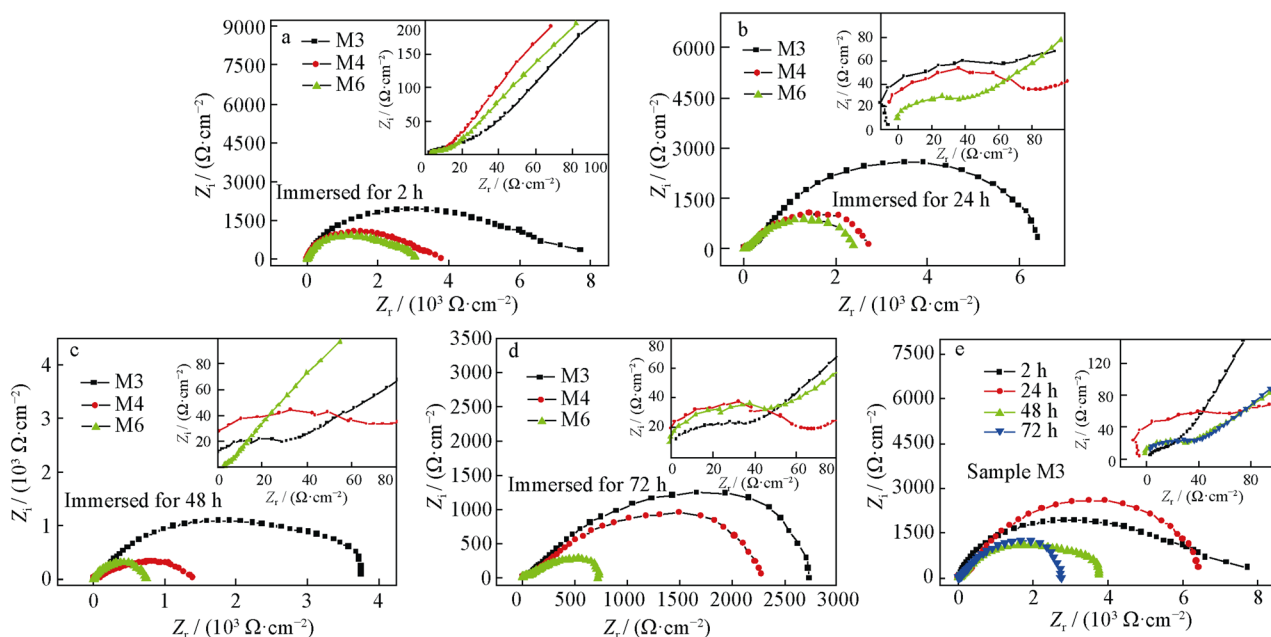


Fig. 3 Nyquist plots of Samples M3, M4 and M6 immersed in HBSS for **a** 2 h, **b** 24 h, **c** 48 h and **d** 72 h; and **e** Nyquist plots of Sample M3 immersed in solution for different time

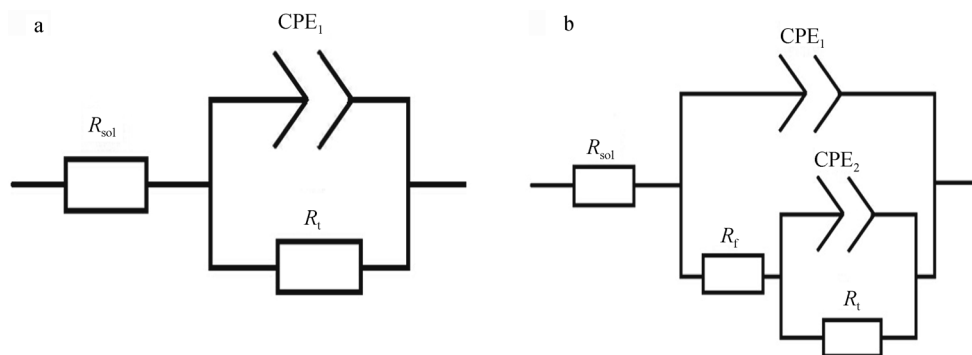


Fig. 4 Equivalent circuit of 2 h **a** and equivalent circuit of 24, 48 and 72 h **b**

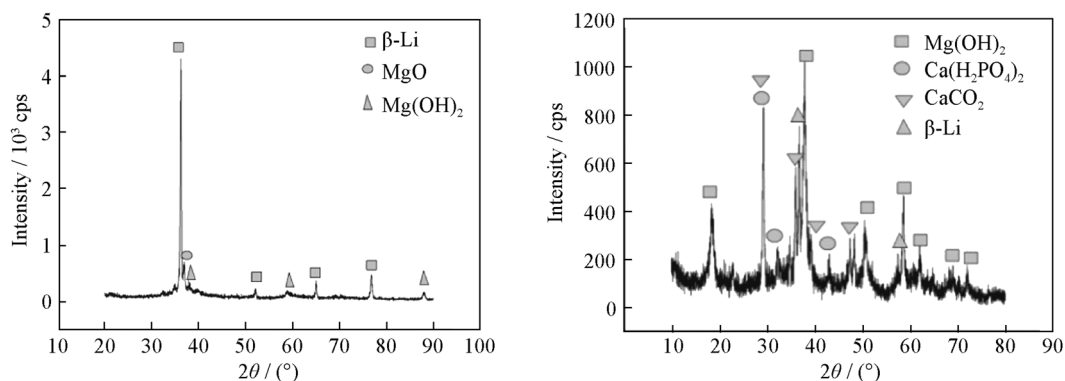


Fig. 5 XRD patterns of Mg-13Li-X alloy after immersion for **a** 2 h and **b** 72 h

of RSP Mg-13Li-X alloy in HBSS changes comparatively little as the immersion time increases. A similar result is observed from the Nyquist impedance plots for Samples M4 and M6 in which an increase in immersion time also leads to a decrease in size of the capacitive loops.

Figure 4 shows the equivalent circuits used to simulate the impedance plots for different immersion time in HBSS. The capacitive loops for impedance plots after immersion for 2 h are simulated by utilizing a simple Randles circuit (Fig. 4a) consisting of electrolyte resistance (R_{sol}), a constant phase element (CPE_1) and the transfer charge resistance (R_t). In order to simulate the impedance plots with immersing time of 24, 48 and 72 h, a film resistance factor (R_f) and another constant phase element (CPE_2) are added in the Randles circuit (Fig. 5b).

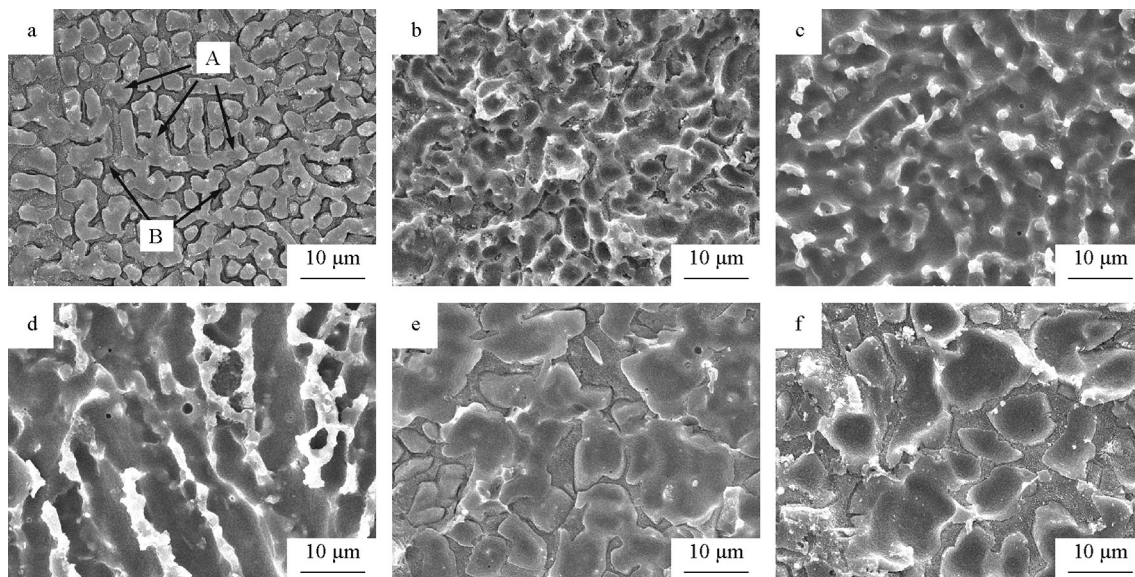
Table 3 shows the fitting values of R_{sol} , CPE_1 , n_1 , R_f , CPE_2 , n_2 and R_t obtained from the impedance data and the equivalent circuits. n_1 and n_2 are parameters of equivalent element; when they are equal to 1, the simulated values are more corrected. Those fitting values are obtained for Samples M3, M4 and M6 in HBSS after immersion for 2, 24, 48 and 72 h. It can be observed from Table 3 that the transfer charge resistance (R_t) values decrease with the

increase in the grain size of each sample for all immersion time. This result is consistent with the results from impedance plots. Compared with the transfer charge resistance (R_t) values, the film resistance (R_f) values are far smaller and those values have the same variation tendency with the transfer charge resistance (R_t).

When the surface of alloy is in contact with HBSS, Cl^- promotes the corrosion process and make it easier for Mg^{2+} to enter the corrosion medium at sites of preferred dissolution. At the same time, OH^- are produced due to hydrogen gas formation from cathodic reaction associated with the electrochemical dissolution of Mg to form Mg^{2+} . The existence of OH^- results in an increase in pH at the interface and promotes the formation of the corrosion products. In the case of samples after immersion for 2 h, on account of the short time of exposure to the environment, the surface of these samples does not have sufficient time to generate a layer of $Mg(OH)_2$. By contrast, in the case of samples after immersion for 24, 48 and 72 h, a layer of corrosion products is formed over the surface of these samples. However, the corrosion product layer could not provide strong protection because of its loose and uncompact microstructure. This explanation is consistent

Table 3 Equivalent circuit parameters of RSP Mg–13Li–X alloy with different immersion time

Time/h	Samples	R_{sol}/Ω	$CPE_1/(\mu F \cdot cm^{-2})$	n_1	R_f/Ω	$CPE_2/(\mu F \cdot cm^{-2})$	n_2	R_t/Ω
2	M3	2.764	4.1960×10^{-5}	0.8563	–	–	–	7649
	M4	5.565	2.3100×10^{-5}	0.8678	–	–	–	3438.0
	M6	5.661	3.4960×10^{-5}	0.9201	–	–	–	3041.0
24	M3	1.223	1.6090×10^{-7}	1.0000	156.7	3.344×10^{-5}	0.8270	7234.0
	M4	1.446	7.9950×10^{-8}	1.0000	88.56	3.304×10^{-5}	0.8543	5545.0
	M6	9.999	9.7190×10^{-8}	1.0000	84.73	2.674×10^{-5}	0.9089	2593.0
48	M3	1.127	1.9930×10^{-7}	1.0000	77.82	6.742×10^{-5}	0.8611	3978.0
	M4	1.191	7.0236×10^{-8}	1.0000	41.86	1.170×10^{-4}	0.9600	1397.0
	M6	2.822	1.0120×10^{-8}	1.0000	14.36	3.311×10^{-5}	0.8807	786.4
72	M3	1.451	8.0840×10^{-8}	1.0000	71.44	1.129×10^{-4}	0.8884	3242.0
	M4	8.851	2.9580×10^{-7}	0.9317	62.68	2.287×10^{-5}	0.9328	904.8
	M6	16.940	1.3210×10^{-7}	1.0000	50.88	4.134×10^{-5}	0.8563	832.3

**Fig. 6** SEM images of Mg–13Li–X alloy without corrosion products: **a** M3 after immersion for 24 h, **b** M3 after immersion for 48 h, **c** M4 after immersion for 24 h, **d** M4 after immersion for 48 h, **e** M6 after immersion for 24 h, and **f** M6 after immersion for 48 h

with the impedance data and the values of the components of the equivalent circuit.

3.4 Corrosion products and microstructural characterization

Figure 5 shows XRD patterns of Mg–13Li–X alloy after immersion for 2 and 72 h. In Fig. 5a, $Mg(OH)_2$ and MgO are the main constituents of the corrosion products after immersion for 2 h. However, Fig. 5b shows a different result. The majority of corrosion products are $Mg(OH)_2$, $Ca(H_2PO_4)_2$ and $CaCO_3$. In summary, $Mg(OH)_2$ is the most common corrosion product for all samples with different immersion times.

In Fig. 6a, Area A is the primary phase and Area B is the eutectic phase. It is apparent that the eutectic phase corrodes before the primary phase because the eutectic phase has many alloying elements, such as Al, Zn and Ca, and these elements could constitute a virtual battery to increase the corrosion rate. Another reason may be that eutectic phase is generated during the last period of solidification and there is no remaining liquid alloy, so the microstructure of eutectic phase is less compact than that of primary phase. Figure 6b shows that corrosion products form on the surface of the eutectic phase. This corrosion product layer can protect the eutectic phase from further attack, so the corrosion process resumes on the surface of the primary phase. Figure 6c–f confirms this hypothesis. Since the

solidification rate of Samples M4 and M6 is slower than that of Sample M3, the area of the eutectic phase in Sample M3 is smaller than that in Samples M4 and M6. The extent of corrosion becomes more serious with solidification rate decreasing. Thus, Sample M3 has the best corrosion performance compared to Samples M4 and M6. This observation also indicates that the mechanism of corrosion is uniform attack rather than pitting attack.

4 Conclusion

The rapid solidification process was observed to refine the grain size of the Mg–13Li–X alloy. The mean grain sizes of RSP Mg–13Li–X alloy are 4.2, 8.2 and 12.7 μm with solidification rate decreasing, respectively. The sample with 4.2 μm in grain size has the most positive E_{corr} (-1.354 V) and the minimum I_{corr} ($5.830 \times 10^{-7}\text{ A}\cdot\text{cm}^{-2}$) after immersion for 2 h. Therefore, the finest grain size sample with the most rapid solidification rate can improve polarization resistance, reduce the corrosion current densities and increase the corrosion resistance in HBSS. The corrosion mechanism of the Mg–13Li–X alloy is uniform attack rather than pitting corrosion.

Acknowledgments This work was financially supported by the National Natural Science Foundation of China (No. 81270116).

References

- [1] Plummer JD, Figueroa IA, Todd I. Phase stability, microstructure and mechanical properties of Li containing Mg-based bulk metallic glass composites. *Mater Sci Eng A*. 2012;546(6):103.
- [2] Gao P, Xue Z, Liu G, Zhang J, Zhang M. Effects of Zn on the glass forming ability and mechanical properties of MgLi-based bulk metallic glasses. *Non-Cryst Solids*. 2012;358(1):8.
- [3] Wu CS, Zhang Z, Cao FH, Zhang LJ, Zhang JQ, Cao CN. Study on the anodizing of AZ31 magnesium alloys in alkaline borate solutions. *Appl Surf Sci*. 2007;253(8):3893.
- [4] Witte F, Fischer J, Nellesen J, Crostack H, Kaese V, Pisch A, Beckmann F, Windhagen H. In vitro and in vivo corrosion measurements of magnesium alloys. *Biomaterials*. 2006;27(7):1013.
- [5] Nagels J, Stokdijk ML, Rozing PM. Stress shielding and bone resorption in shoulder arthroplasty. *J Shoulder Elb Surg*. 2003;12(1):35.
- [6] Liu D, Wu B, Wang X, Chen M. Corrosion and wear behavior of an Mg–2Zn–0.2Mn alloy in simulated body fluid. *Rare Met*. 2015;34(8):553.
- [7] Xu L, Yu G, Zhang E, Pan F, Yang K. In vivo corrosion behavior of Mg–Mn–Zn alloy for bone implant application. *J Biomed Mater Res A*. 2007;83A(3):703.
- [8] Chang T, Wang J, Chu C, Lee S. Mechanical properties and microstructures of various Mg–Li alloys. *Mater Lett*. 2006;60(27):3272.
- [9] Chusid O, Gofer Y, Gizbar H, Vestfrid Y, Levi E, Aurbach D, Riech I. Solid-state rechargeable magnesium batteries. *Adv Mater*. 2003;15(78):627.
- [10] Luo S, Zhang Q, Zhang Y, Chao L, Xu X, Zhou T. In vitro and in vivo studies on a Mg–Li–X alloy system developed as a new kind of biological metal. *Mater Sci Forum*. 2012;747(18):257.
- [11] Ballerini G, Bardi U, Bignucolo R, Ceraolo G. About some corrosion mechanisms of AZ91D magnesium alloy. *Corros Sci*. 2005;47(9):2173.
- [12] Verdier S, van der Laak N, Delalande S, Metson J, Dalard F. The surface reactivity of a magnesium-aluminium alloy in acidic fluoride solutions studied by electrochemical techniques and XPS. *Appl Surf Sci*. 2004;235(4):513.
- [13] Yamasaki M, Hayashi N, Izumi S, Kawamura Y. Corrosion behavior of rapidly solidified Mg–Zn–rare earth element alloys in NaCl solution. *Corros Sci*. 2007;49(1):255.
- [14] Liang J, Hu L, Hao J. Characterization of microarc oxidation coatings formed on AM60B magnesium alloy in silicate and phosphate electrolytes. *Appl Surf Sci*. 2007;253(10):4490.
- [15] Yamauchi N, Ueda N, Okamoto A, Sone T, Tsujikawa M, Oki S. DLC coating on Mg–Li alloy. *Surf Coat Technol*. 2007;201(9–11):4913.
- [16] Zeng R, Sun L, Zheng Y, Cui H, Han E. Corrosion and characterization of dual phase Mg–Li–Ca alloy in Hank's solution: the influence of microstructural features. *Corros Sci*. 2014;79:69.
- [17] Song G, Atrens A, Dargusch M. Influence of microstructure on the corrosion of diecast AZ80D. *Corros Sci*. 1999;41(18):249.
- [18] Li Y, Zhang T, Wang F. Effect of microcrystallization on corrosion resistance of AZ91D alloy. *Electrochim Acta*. 2006;51(14):2845.
- [19] Makar GL. Corrosion studies of rapidly solidified magnesium alloys. *J Electrochem Soc*. 1990;137(2):414.
- [20] Zhao Y, Zhao X. Structural relaxation and its influence on the elastic properties and notch toughness of Mg–Zn–Ca bulk metallic glass. *J Alloys Compd*. 2012;515(15):154.
- [21] Huan ZG, Leefflang MA, Zhou J, Fratila-Apachitei LE, Duszczyk J. In vitro degradation behavior and cytocompatibility of Mg–Zn–Zr alloys. *J Mater Sci Mater Med*. 2010;21(9):2623.
- [22] Jiang B, Zeng Y, Yin H, Li R, Pan F. Effect of Sr on microstructure and aging behavior of Mg–14Li alloys. *Prog Nat Sci Mater Int*. 2012;22(2):160.
- [23] Wu L, Cui C, Wu R, Li J, Zhan H, Zhang M. Effects of Ce-rich RE additions and heat treatment on the microstructure and tensile properties of Mg–Li–Al–Zn-based alloy. *Mater Sci Eng A*. 2011;528(4–5):2174.
- [24] Zhang Y, Luo S, Zhang Q. Microstructures and mechanical properties of a new biomedical material Mg–13Li–X alloys. *Mater Sci Forum*. 2013;747:251.
- [25] Zhang C, Huang X, Zhang M, Gao L, Wu R. Electrochemical characterization of the corrosion of a Mg–Li alloy. *Mater Lett*. 2008;62(14):2177.